ROYAL SOCIETY OF CHEMISTRY

Check for updates

Electronic, mechanical and piezoelectric properties of glass-like complex Na₂Si₁₋ₓGeₓO₃ (x = 0.0, 0.25, 0.50, 0.75, 1.0)

R. Zosiamliana,[ab] B. Chettri,[ac] G. S. L. Fabris, [ID][d] J. R. Sambrano, [ID][e] Sherzod Abdullaev, [ID][fg] G. Abdurakhmanov [ID][*h] and D. P. Rai [ID][*a]

Motivated by our previous work on pristine Na₂SiO₃, we proceeded with calculations on the structural, electronic, mechanical and piezoelectric properties of complex glass-like Na₂Si₁₋ₓGeₓO₃ (x = 0.0, 0.25, 0.50, 0.75, 1.0) by using density functional theory (DFT). Interestingly, the optimized bond lengths and bond angles of Na₂SiO₃ and Na₂GeO₃ resemble each other with high similarity. On doping we report the negative formation energy and feasibility of transition of Na₂SiO₃ → Na₂GeO₃ while the structural symmetry is preserved. Analyzing the electronic profile, we have observed a reduced band gap on increasing x = Ge concentration at Si-sites. All the systems are indirect band gap (Z−Γ) semiconductors. The studied systems have shown mechanical stabilities by satisfying the Born criteria for mechanical stability. The calculated results have shown highly anisotropic behaviour and high melting temperature, which are a signature of glass materials. The piezoelectric tensor (both direct and converse) is computed. The results thus obtained predict that the systems under investigation are potential piezoelectric materials for energy harvesting.

1 Introduction

Wide band gap semiconductor materials have attracted a great deal of attention due to the possibility of band gap engineering, either by doping with heavier elements or by making oxygen vacancy defects so as to improve their performance towards different applications and different tasks.[1,2] In recent years, theoretical and experimental insight into novel silica (SiO₂) based glass-like materials has become a fascinating topic among researchers due to their high mechanical as well as thermodynamical stability, low thermal conductivity and abundance in nature.[3,4] Further refinements of such properties through the manufacturing processes and chemical compositions have improved their thermal, pressure and chemical

[a]*Department of Physics, Physical Sciences Research Center (PSRC), Pachhunga University College, Mizoram University, Aizawl-796001, India. E-mail: dibya@pucollege.edu.in*

[b]*Department of Physics, Mizoram University, Aizawl-796004, India*

[c]*Department of Physics, North-Eastern Hill University, Shillong-793022, Meghalaya, India*

[d]*Postgraduate Program in Materials Science and Engineering, Federal University of Rio Grande do Norte, 59078-970 Natal, RN, Brazil*

[e]*Modeling and Molecular Simulation Group, Sao Paulo State University Julio de Mesquita Filho, Bauru, SP, Brazil*

[f]*Andijan Machine-Building Institute, Andijan, Uzbekistan. E-mail: editory1001@gmail.com*

[g]*"Editory" LLC, Tashkent, Uzbekistan*

[h]*National University of Uzbekistan, 4 Universitet str., 100174 Tashkent, Uzbekistan. E-mail: gulmirzo@mail.ru*

resistivity, and transparency, which has made them reliable and suitable materials for different applications and feasible materials for a wide range of devices.[5–13] As far as we are aware, within the surveyed literature most of the important glasses are silicate glass having high content of silica (SiO₂) or quartz.[14–16] As reported, silicate glasses have high technological importance in industry and in commercial applications: battery and storage systems, opto-electronic devices, and auxetic materials having high performances in the fields of bio-medicine, surgical implants and piezoelectric sensors and actuators, fireproof fabrics, optical fibres, lighting technology, and many more.[17–21] The pioneering work of Randall *et al.*[22] suggested that silicate glass structures were thought to be well understood at a local level and reported that vitreous silica probably consists of small crystals of cristobalite that were formed at very high temperatures by performing an experimental investigation using X-ray diffraction (XRD). Zachariasen *et al.*[23] have investigated heat-treated specimens by using XRD and reported a complex silicate glass structure. The vitreous forms of silica showed the relative orientation of two oxygen tetrahedra to form a network of SiO₂ characterized by an extended three dimensional network which lacked symmetry and periodicity. The structure was well delineated by the continuous random network (CRN). It was also reported that the network of vitreous silica was built up of oxygen tetrahedra that surround the silicon atom. However, in the vitreous form of silica, the relative orientation of two tetrahedra with a common corner may vary within a wide limit and oxygen to oxygen atom bond angles may also vary throughout the whole network. Thus, the glassy phases of SiO₂

that consist of Si–O tetrahedra nonetheless have bond-angle disorder both in O–Si–O and Si–O–Si angles.[23–26]

The structural profile and the atomic arrangement of silicate glasses are well investigated by both experimental and computational methods.[27–30] The most common superlative experimental set-ups employed for determination of many fingerprints of the structures were: Raman spectroscopy, extended X-ray absorption fine structure (EXAFS) spectroscopy, nuclear magnetic resonance (NMR), neutron diffraction and so on.[31–40] The experimental studies mainly highlighted the structure of silicate glasses and were mostly defined by the medium range or short range order (MRO or SRO), *i.e.*, the order over distances comparable to inter-atomic distances, and lacked long-range order (LRO) leading to more complications and challenges when examining the structural properties. In alkali-silicates such as Na_2SiO_3, the Na^+ cations progress towards the non-bridging oxygen (NBO) making weak ionic bonds that result in the formation of sodium *meta*-silicate. The NBO in the structure comprises one half of the permanently broken oxygen bond due to the alkali Na^+ ions that destroy the Si–O–Si bridging bonds (BO).[41–43] Experimental work on sodium oxide-silica obtained from the sodium–concrete reaction (SCR) method and XRD measurement have revealed the formation of Na_2SiO_3 *etc.*[44] As a matter of fact, the experimental works are limited to structural and electronic studies. In order to analyze the desired functional properties and investigate these materials at the atomic-scale, computational methods have become a major tool. Computational techniques such as reverse Monte Carlo, *ab initio* molecular dynamics (AIMD) based on density functional theory (DFT) and classical molecular dynamics (MD) are the most frequently employed simulation methods for such investigations.[45–47] More recently, methods that include pre-available experimental data such as force enhancement atomic refinement (FEAR) have been used by Pandey *et al.*[48] for structural modeling of amorphous Si and SiO_2 using the reverse Monte Carlo approach where they acquired authentic structures.

The structure of Na_2GeO_3 was first determined by Ginetti[49] who revealed the crystal structure of Na_2GeO_3 by means of radio-crystallographic study with residual factor $(R) = 28\%$. Later refinement was carried out by Vollenkle *et al.*[50] with $R = 4.4\%$ and the mean Ge–O distances in the Na_2GeO_3 chain were found to be 1.836 Å for the bridging oxygen atom and 1.713 Å for the terminal oxygen atom and an average value of 2.39 Å was calculated for the Na–O distances. A recent experimental work on the preparation of Na_2GeO_3 was reported by Cruickshank[51] by re-growing the crystals and collected 1083 reflexions by using a Syntex diffractometer. From this work, it was observed that pristine Na_2GeO_3 existed in an orthorhombic crystal structure with space group $Cmc2_1$ and the mean bond lengths of Ge–O (bridging) = 1.800 Å and Ge–O (non-bridging) = 1.712 Å, and Ge–O–Ge bond angle = 124.6°. Moreover, system transformation of $Li_2GeO_3 \rightarrow Na_2GeO_3$ and $Li_2SiO_3 \rightarrow Na_2SiO_3$ was reported by West *et al.*[52] where the starting compounds were reagent grade Li_2CO_3 and Na_2CO_3, and electronic grade GeO_2. The mixture was then heated in an electric muffle furnace at 850 °C and the final product of the reaction was checked by using Guinier X-ray powder methods.

As far as we know, the theoretical and experimental insights into the structural and electronic properties of Na_2SiO_3 are well explored.[53] So, in this work, the main focus of the study will be investigation of the transformation of $Na_2SiO_3 \rightarrow Na_2GeO_3$ and the modulation of the electronic and mechanical properties by Ge doping at Si-sites using DFT.

2 Computational details

The computational simulations and calculations were performed within the framework of density functional theory (DFT) using the linear combination of Gaussian-type functions (GTF) to describe the crystal orbitals, as implemented in the CRYSTAL17 code,[54] adopting the Perdew–Burke–Ernzerhof (PBE) exchange–correlation functional.[55] The sodium (Na), silicon (Si) and oxygen (O) atomic centers were described by a revised triple-zeta valence plus polarization (TZVP) basis set, developed by Oliveira *et al.*,[56] and the dopant, *i.e.*, germanium (Ge) was described by a TZVP basis set developed by Peintinger and co-workers.[57] For the structural optimization, the accuracy of the convergence criteria for the bi-electronic integrals was controlled by a set of five thresholds $(10^{-7}, 10^{-7}, 10^{-7}, 10^{-7}, 10^{-14})$, and these represent the overlap and penetration for Coulomb integrals, the overlap for HF exchange integrals, and the pseudo-overlap, respectively. The energy convergency was considered when the energy difference of two consecutive thresholds was lower than 10^{-7} Ha, and the shrinking factor (Pack–Monkhorst and Gilat net) was set to 12 × 12 × 12.[58] The structural convergence was checked on the gradient components and nuclear displacements with tolerances on their root mean square set to 0.0001 and 0.0004 a.u., respectively.

All stationary points were characterized as minima by diagonalizing the Hessian matrix with respect to atomic coordinates and unit cell parameters, and analyzing the vibrational phonon modes at the high-symmetry points of the first Brillouin zone,[58] using the numerical second derivatives of the total energies estimated with the coupled perturbed Hartree–Fock/Kohn–Sham algorithm. Also, it is worth highlighting that the electronic properties extracted were obtained using the same *k*-point sampling employed for the diagonalization of the Fock matrix in the optimization process. The pristine sodium silicate consists of a unit cell of 12 atoms, which contains 4 sodium (Na), 2 silicon (Si) and 6 oxygen (O) atoms, which have an orthorhombic phase symmetry, and belongs to the $Cmc2_1$ space group,[27,28,59] and has experimental lattice parameters $a = 10.480$ Å, $b = 6.070$ Å and $c = 4.820$ Å [see Table 1]. To model and study $Na_2Si_{1-x}Ge_xO_3$, with the concentration of Ge, $x = 0, 0.25, 0.50, 0.75$ and 1.0, a 2 × 1 × 1 supercell was built that contains 24 atoms. Each of the doped systems were optimized to investigate the structural, electronic, mechanical and piezoelectric properties.

3 Results and discussion

3.1 Structural properties and dynamical stabilities

In this section, we discuss the structural properties of sodium silicate upon performing doping with germanium (Ge) on the silicon (Si) site. As previously mentioned in the Computational

Table 1 Calculated optimised lattice parameters of the Na_2SiO_3 unit cell (12-atoms) compared to B3LYP (Belmonte et al.[28]), PBE (Cuautli et al.[29]), LDA (Liu et al.)[30] and experimental values (McDonald et al.[27]). Here, the relative errors are calculated with respect to the experimental data

Parameters	PBE-GGA (this work)	B3LYP[28]	PBE[29]	LDA[30]	Exp.[27]
a (Å)	10.683 ± 1.94	10.568	10.630	10.446	10.480
b (Å)	6.172 ± 1.68	6.098	6.160	6.030	6.070
c (Å)	4.892 ± 1.49	4.852	4.880	4.710	4.820
V (Å^3)	322.559 ± 5.01	312.681	319.546	296.680	306.60

details section, it has to be noted that, as the constructed supercells are asymmetric supercells (i.e., supercells of $2 \times 1 \times 1$ such that the number of atoms is 24 atoms), the optimised structures for all different percentage doping levels given as $Na_2Si_{1-x}Ge_xO_3$ ($x = 0.0$, 0.25, 0.50, 0.75, 1.0) are in the lowest possible primitive symmetry with space group $P1$, since the building of the supercell affects the environment of the atoms in a certain direction. Fig. 1 shows the emergence of different doped structures via the supercell method along the x-axis. It has not only lowered the symmetry to the triclinic $P1$ space group but also has a large effect on the lattice parameter 'a', while the effect on 'b' and 'c' is almost negligible (see Table 2). It is obvious that whenever doping with heavier atoms is performed on a crystal structure, the lattice parameters along all the axes should increase due to the larger atomic radius of the dopant atom (i.e., the atomic size of Ge is larger than that of Si). This study has elucidated the increase in lattice parameters with the increase in doping concentration [see Fig. 2].

To obtain the most stable structure of all the systems we have calculated the total energy corresponding to each unit cell volume (lattice parameters). The data of total energy and unit cell volume are fitted to the Birch–Murnaghan equation of states to obtain a smooth parabolic curve as shown in Fig. 3. The Birch–Murnaghan equation[60,61] is given as

$$E(V) = E_0 + \frac{9 \times B_0 V_0}{16} \left[\left[\left(\left(\frac{V_0}{V} \right)^{\frac{2}{3}} - 1 \right)^3 \times B'_0 + \left[\left(\frac{V_0}{v} \right)^{\frac{2}{3}} - 1 \right]^2 \right. \\ \left. \times \left[6 - 4 \times \left(\frac{V_0}{V} \right)^{\frac{2}{3}} \right] \right]$$
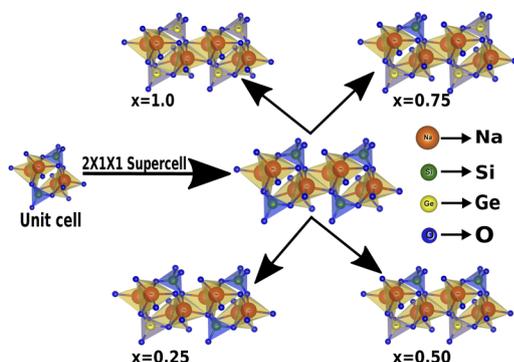
(1)

Fitting the smooth curve from the equation of states at temperature = 0 K and pressure = 0 GPa gives the optimized lattice parameters including the cell bulk modulus. The bulk modulus (B) evaluates the magnitude of the average bond strength in the crystal. The bulk modulus decreases with the increase in doping concentration, which indicates a reduction in the average valence bond strength [see Tables 3 and 4]. The optimized result of Na_2SiO_3 with 12 atoms in the unit cell is in the orthorhombic $Cmc2_1$ space group and in good agreement with the previously reported results.[27–29,51] The optimised lattice parameters are $a = 10.683$ Å, $b = 6.172$ Å and $c = 4.892$ Å, with an optimised volume of $V = 322.559$ Å^3. The calculated lattice parameters 'a', 'b' and 'c' are comparable to those of the previously reported theoretical results from PBE as the exchange correlation functional,[29,53] the Becke 3-parameter,[28] the Lee–Yang–Parr (B3LYP) functional,[30] and the experimental data obtained by McDonald et al.[27]

For further confirmation of the structural stability we have calculated the formation energies (E_{form})[62] by using eqn (2) given below

$$E_{form} = \frac{1}{24} \left(E_x^{total} - \sum n_z E_z^{bulk} \right)$$

(2)

where z indicates the number of atoms (Na, Si, Ge, O) and $x = 0.0$, 0.25, 0.50, 0.75, 1.0. The negative values of the calculated formation energies revealed the ground state structural stability of all the systems which implies the realization of experimental synthesis. The magnitude of E_{form} decreases as the doping concentration increases, which indicates the instability of doped structures.

The comparative results of the optimized lattice parameters and the previously reported data are tabulated in Table 1. From Table 1, it can be seen that our calculated volume is 3.06%, 0.93%, 8.02% and 4.95% larger than those reported by Belmonte et al.,[28] Cuautli et al.,[29] Liu et al.[30] and McDonald

Fig. 1 Building the asymmetric supercell of $2 \times 1 \times 1$ from the Na_2SiO_3 unit cell and doping the Si site with Ge.

Table 2 Calculated lattice parameters in Å and the change in lattice parameters of the supercell structure with 12-atoms in Å under different doping concentrations

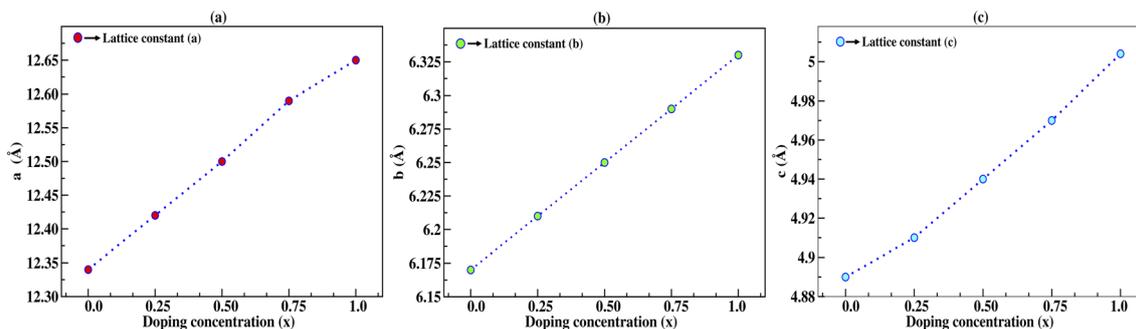| Doping concentration (x)	a	b	c	Δa	Δb	Δc
Unit cell	10.683	6.172	4.892	0	0	0
0.0	12.337	6.168	4.892	1.654	−0.004	0
0.25	12.414	6.209	4.912	1.731	0.037	0.020
0.50	12.502	6.252	4.937	1.819	0.080	0.045
0.75	12.590	6.285	4.964	1.907	0.113	0.072
1.0	12.651	6.325	5.004	1.968	0.153	0.112

Fig. 2 Lattice constants *a*, *b*, and *c* in Å as a function of doping concentration (*x*) of germanium (Ge), where the lattice constants increase with increasing doping concentration.
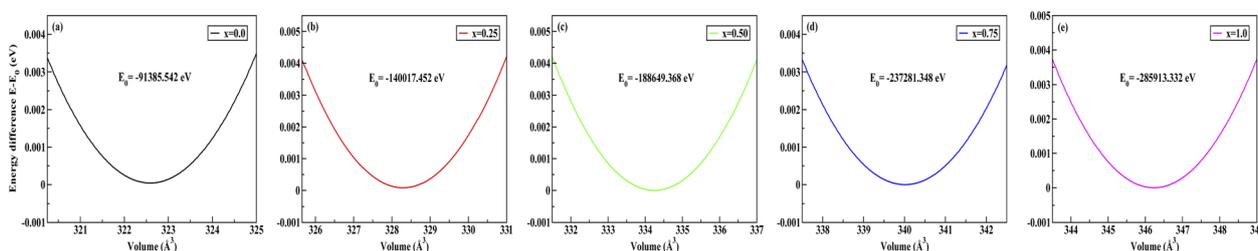

Fig. 3 Difference in energy ($E - E_0$) eV *versus* volume (Å³) graphs from equation of state calculations adopting Birch–Murnaghan fitting for obtaining the most stable optimized volume at *x* = (a) 0.0, (b) 0.25, (c) 0.50, (d) 0.75, (e) 1.0. E_0 indicates the minimum ground state energy.

et al.[27] respectively. The dissimilarities of volumes are due to the well-known effect of the PBE exchange–correlation in the GGA.

In the glassy phases of silica (SiO_2) and germanium dioxide (GeO_2) containing Na_2O, the structural hallmarks are the presence of tetrahedral chains.[63,64] The existence of Na_2O

Table 3 Calculated bond lengths (in Å) and bond angles (in °) of $Na_2Si_{1-x}Ge_xO_3$. Here, O → bridging oxygen, O′ → non-bridging oxygen and x is the doping concentration[a]

		x				
Structural parameters	Unit cell (12 atoms)	0	0.25	0.50	0.75	1.0
Bond length (in Å)						
Si–O	1.73	1.73	1.73	1.74	1.74	—
	1.672*[a]					
Si–O′	1.64	1.64	1.64	1.64	1.64	—
	1.592*[a]					
Ge–O	—	—	1.85	1.85	1.86	1.86
						1.80*[b]
Ge–O′	—	—	1.75	1.75	1.75	1.75
	—					1.721*[b]
O–O	2.68					
	2.619*[a]					
O′–O′	2.81					
	2.714*[a]					
Bond angle (in °)						
O′–Si–O′	117.6	117.6	117.9	117.7	117.7	—
	116.89*[a]					
O–Si–O′	106.3	106.3	106.3	106.2	106.2	—
	107.07*[a]					
O′–Ge–O′	—	—	118.5	118.7	118.5	118.8
						118.9*[b]
O–Ge–O′	—	—	105.1	105.3	105.2	105.2
						105.6*[b]

[a] *[a] and *[b] represent ref. 27 and 51 respectively.

Table 4 Calculated formation energies (E_{form}) and bulk modulus (B) for $Na_2Si_{1-x}Ge_xO_3$ (x = 0.0, 0.25, 0.50, 0.75, 1.0) calculated from the equation of states at T = 0 K and P = 0 GPa, and their corresponding changes with respect to x = 0.0

x	E_{form} (in eV)	B (in GPa)	$|\Delta E_{form}|$	$|\Delta B|$
0.0	−2.478	62.26	0	0
0.25	−2.407	60.00	0.071	2.26
0.50	−2.336	58.91	0.142	3.35
0.75	−2.267	56.75	0.211	5.51
1.0	−2.198	54.87	0.28	7.39

depolymerizes the tetrahedral chain networks by breaking the Si–BO–Si and Ge–BO–Ge bonds, forming non-bridging oxygen (NBO) atoms.[65,66] To understand the atomic arrangement inside the unit cells for different doping concentrations and the pristine compound (unit cell with 12 atoms), we have calculated the bond lengths and bond angles for both BO and NBO as presented in Table 3. We report the negligible deformation of bond lengths and bond angles while increasing the Ge concentration, confirming the structural similarities between Na_2SiO_3 and Na_2GeO_3. Similar findings have been reported by Cruickshank.[51] From Table 3, we have noticed the larger bond lengths of X–BO as compared to X–NBO (where X = Si or Ge). This may be attributed to excess charge transfer to NBO, one of the characteristic features of glass silica. In sodium silicate and sodium germanate, the presence of electropositive cations minimized the bonding potentials, resulting in an appreciable difference in the lengths of bridging and non-bridging bonds. Also, our calculations show that the BO–BO and NBO–NBO bond lengths are consistent throughout the doping concentrations and these bond lengths are comparable to the experimental results [see Table 3].

In order to probe the dynamical stability of the compounds, the phonon dispersion curves along the high symmetry Γ, X, R, Z, Y, Γ directions in the Brillouin zone (BZ) are calculated as shown in Fig. 4. Since the unit cell consists of 24 atoms for each doped system, we obtain 72 branches in the phonon dispersion curve. Clearly from Fig. 4, all the phonon modes are real which suggests the dynamical stability of the studied phases against any arbitrary finite displacement of the atoms about their mean positions.

3.2 Electronic properties

Insight into the atomic-scale interactions in any material is provided by the electronic properties. In this section, we present the detailed investigations of the electronic properties of $Na_2Si_{1-x}Ge_xO_3$ by calculating the band structures and the density of states (DOS) [see Fig. 5 and 6]. Our results are in good agreement with the previously reported ones.[25,30,42,65,67] From Fig. 5, we can see a small dispersion at the top of the valence band regions (VB), while for the bottom of the conduction band regions (CB), the electronic bands are largely dispersed for all different doping concentrations. The top of the valence band lies close to the Fermi energy (E_F), suggesting p-type semiconducting behaviour. For all concentrations, the highest energy state of the valence band is located at the Z-symmetry point while the lowest energy state of the conduction band is at the Γ-symmetry point. The presence of Z–Γ-symmetry in all doped systems indicates an indirect bandgap semiconductor. Our studies agreed well with the previously reported results of Lui et al.[30] for the ab initio total-energy obtained with the local density approximation (LDA) via a preconditioned conjugate gradient algorithm. Recently, Baral et al.[42] reported the electronic structure calculations of $(Na_2O)_x(SiO_2)_{1-x}$ (x = 0.0, 0.1, 0.2, 0.3, 0.4, 0.5) by using the VASP code adopting the orthogonal linear combination of atomic orbitals (OLCAO) approach and reported a decrease in band gap from 5.657 eV to 2.60 eV on increasing the x value. Subedi et al.[65] have reported electronic band gaps (E_g) of 3.96 and 3.82 eV for $(Na_2O)_x(SiO_2)_{1-x}$ at x = 0.1 and 0.3 respectively. Our calculated indirect band gap (Z–Γ-symmetry) of Na_2SiO_3 is found to be 3.908 eV. However, the experimental band gap was found to be 6.0 eV for silicate glass.[68] Ching et al.[67] have highlighted the sensitiveness of the band gap towards the exchange parameters. The calculated E_g of Na_2SiO_3 were found to be 6.46 eV and 9.98 eV for $\alpha = \frac{2}{3}$ and $\alpha = 1.0$ parameters, respectively. Thus the discrepancy that arises in the band gap calculation is due to the choice of different exchange parameters. Referring to Fig. 7, it is clear that with the increase in doping concentration, the E_g gradually decreases to a minimum value of E_g = 3.1327 eV. It is obvious that doping of any materials with heavier elements should reduce the band gap and enhance the mobility of electrons between the VB and CB due to the introduction of extra bands near the Fermi level. Interestingly, for even doping
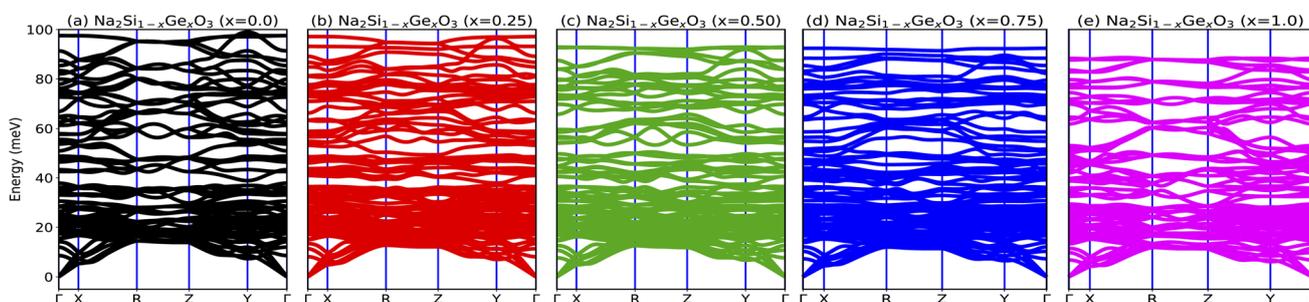

Fig. 4 (a–e) Phonon dispersion curves of $Na_2Si_{1-x}Ge_xO_3$ (x = 0.0, 0.25, 0.50, 0.75, 1.0), which show positive values for all x, indicating the materials' dynamical stability.

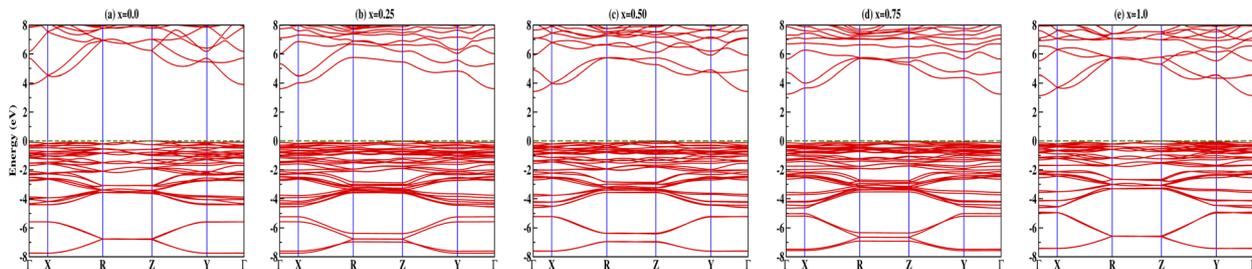**Fig. 5** Calculated band structures of $Na_2Si_{1-x}Ge_xO_3$: (a) $x = 0.0$, (b) $x = 0.25$, (c) $x = 0.50$, (d) $x = 0.75$, and (e) $x = 1.0$.

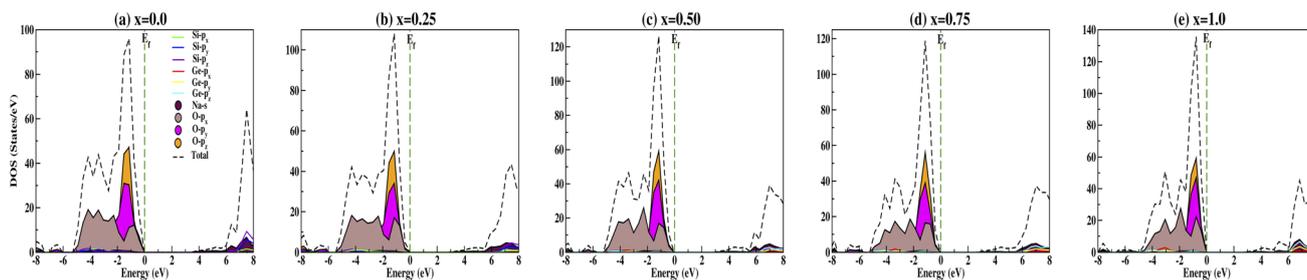**Fig. 6** Partial density of states calculated for $Na_2Si_{1-x}Ge_xO_3$: (a) $x = 0.0$, (b) $x = 0.25$, (c) $x = 0.50$, (d) $x = 0.75$, and (e) $x = 1.0$.

concentrations [see Fig. 5(a, c and e)], we have observed the last two bands of the CB intersecting along the X-symmetry while these characteristics are not visible in odd doping [see Fig. 5(b and d)]. This suggests that for even doping the last two bands of the CB are possibly contributed by the Na-s orbital.

The calculated DOS gives the number of different states at a particular energy level that electrons are allowed to occupy as shown in Fig. 6. Analysis of the DOS plot indubitably reveals that the majority of energy states around the top of the VB are contributed by oxygen O-p_x, O-p_y and O-p_z orbitals while the bottom of the CB is mainly contributed by the silicon Si-p_x, Si-p_y and Si-p_z, and sodium Na-s orbitals for doping concentration $x = 0.0$ [Fig. 6(a)]. From Fig. 6(b–e), we have observed the shifting of the bottom of the conduction band towards the Fermi energy on increasing the concentration of Ge dopant. Recently, Wang *et al.*[69] reported the band gap variation of H_xMoO_3, $0 < x \leq 2$ and observed a quasi-metallic property of H_xMoO_3. Similarly, from the PDOS plot (Fig. 6) we can see that allowed shallow states are created due to Ge dopant atoms near the conduction band minima and observe a more complex hybridization between Na-s, Si-p and Ge-p orbitals, *i.e.*, more orbitals overlap as x increases. This results in the shifting of the conduction region towards the Fermi level and thus reduces the band gap when x increases as shown in Fig. 7. However, within the valence band region, the contributions from Na-s, Si-p and Ge-p orbitals are negligibly small compared to O-p, and as a result the dopant atoms do not have much effect in the valence band region. This enhances the semi-conducting properties of the studied compounds. The oxygen contribution in the VB region was further analyzed in terms of BO and NBO; between -5.5 and 0 eV all the oxygen orbitals O-p_x, O-p_y and O-p_z split into two main regions with the BO peaks at lower

energy. This reveals that the top of the VB is mainly from the NBO contribution due to its higher energy state. Referring to the relative atomic concentration of BO and NBO, the DOS intensity (states per V) of BO should be half that of NBO. From the total DOS (TDOS) calculations within -5.5 eV to 0 eV, for all concentrations the TDOS intensities near the Fermi level (*i.e.*, the contribution from NBO) are almost double the TDOS intensities within the region of -5.5 to -3.0 eV (*i.e.*, the contribution from BO). Ching *et al.*[67] reported that the BO valence orbitals were at lower energy (or higher binding energy) as compared to NBO. This is consistent with the atomic structure of the compounds as the bond lengths of BO–BO are smaller in comparison with NBO–NBO (see Table 3 for O–O and O′–O′ bond lengths). This fact can be explained by on-site Coulomb repulsion; lower energy (or higher binding energy)
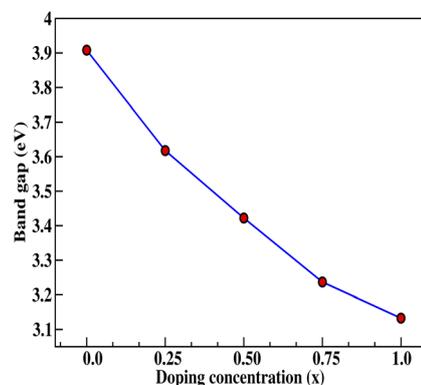

Fig. 7 Calculated band gap (in eV) *versus* doping concentration (x). Here, red dots indicate the corresponding band gaps at $x = 0.0$, 0.25, 0.50, 0.75, 1.0 for doping with Ge on Si sites.

BO valence orbitals should have lower electronic valence charge as compared to NBO. This implies that the electrostatic repulsion between BO–BO is smaller, thus resulting in a smaller separation than that of NBO–NBO.

3.3 Elastic and mechanical properties

To perceive whether the studied compounds meet the required stability and durability, the elastic constants play an important role to determine the strength, response of the compounds towards external stress, and applicability for practical applications. In this regard, we have calculated the elastic constants and other mechanical properties of $Na_2Si_{1-x}Ge_xO_3$. The calculated values at $x = 0.0$ are comparable to an earlier report by Belmonte *et al.*[28] using the LCAO DFT/B3LYP functional. The elastic constant tensors C_{ij} computed using stress–strain relations[70,71] are presented in Table 5; they satisfy the necessary and sufficient Born criteria for a triclinic $P1$ structure,[72,73] *i.e.*, $C_{11} > 0$, $C_{22} > 0$, $C_{33} > 0$, $C_{44} > 0$, $C_{55} > 0$, $C_{66} > 0$ $[C_{11} + C_{22} + C_{33} + 2(C_{12} + C_{13} + C_{23})] > 0$, $C_{33}C_{55} - C_{35}^2 > 0$, $C_{44}C_{66} - C_{46}^2 > 0$ and $C_{22} + C_{33} - 2C_{23} > 0$. This indicates that the compounds under investigation are mechanically stable. The mechanical stability is further confirmed by the positive stiffness eigenvalues (λ). Herein, we have also investigated the phase velocity and polarization of seismic waves along a given propagation direction using the Christoffel determinant:[74]

$$|C_{ijkl}n_jn_l - \rho V^2\delta_{ik}| = 0 \tag{3}$$

where C_{ijkl} are elastic constant tensors, n is the unit vector normal to the surface of seismic propagation into space, ρ is the density of the crystal, V is the phase velocity of the seismic wave and δ_{ik} is the Kronecker delta. From this calculation we obtain two sets of waves: a quasi-longitudinal wave (v_p) and two quasi-shear waves with $v_{s_{fast}} > v_{s_{slow}}$. Here, v_p is polarized nearly along the direction of propagation while the two latter waves are polarized almost perpendicular to the direction of propagation (see Table 6). Utilizing the elastic constant tensor and its compliance tensor (S_{ij}), we perform a calculation of $\bar{V}_{P_{VRH}}$ and $\bar{V}_{S_{VRH}}$ which gives the isotropic seismic velocities averaged over all propagation directions (calculated values of $\bar{V}_{P_{VRH}}$ and $\bar{V}_{S_{VRH}}$ are given in Table 6). The main reason for calculating such parameters is to understand the single-crystal azimuthal seismic anisotropy for longitudinal waves (A_P) and shear waves (A_S) given by:[75]

$$A_P = \left(\frac{v_{p_{max}} - v_{p_{min}}}{\bar{V}_{P_{VRH}}}\right) \times 100 \tag{4}$$

and

$$A_S = \left(\frac{v_{s_{max}} - v_{s_{min}}}{\bar{V}_{S_{VRH}}}\right) \times 100 \tag{5}$$

Table 5 Calculated elastic constants C_{ij} (in GPa units), anisotropic factors (A_{an} and A^U) (unitless), stiffness eigenvalues (λ) (in GPa units), density of the compounds (ρ) (in g cm^{-3}), transverse (v_t), longitudinal (v_l) and average (v_{av}) velocities of sound (in km s^{-1}), and the dimensionless Kleinman coefficient (ζ) for $Na_2Si_{1-x}Ge_xO_3$ ($x = 0.0, 0.25, 0.50, 0.75, 1.0$)

x	C_{11}	C_{22}	C_{33}	C_{44}	C_{55}	C_{66}	C_{12}	C_{13}	C_{23}	A_{an}	A^U
0.0	118.824	100.117	111.436	50.007	35.059	18.086	44.978	28.728	41.368	2.75	0.67
0.25	115.075	96.262	101.447	47.864	34.197	17.770	46.775	30.520	39.525	2.96	0.62
0.50	112.696	94.043	95.406	45.886	33.278	17.288	47.404	29.755	93.827	3.03	0.629
0.75	108.624	90.601	85.019	44.208	32.371	16.544	48.434	32.505	37.800	3.38	0.627
1.0	103.831	89.733	76.126	42.912	31.329	15.570	49.127	34.491	36.838	3.74	0.678

x	λ_1	λ_2	λ_3	λ_4	λ_5	λ_6	ρ	v_t	v_l	v_{av}	ζ
0.0	18.086	35.059	50.007	57.133	86.202	187.04	2.519	3.615	6.491	4.025	0.519
0.25	17.77	34.197	47.822	52.934	77.059	182.83	2.701	3.399	6.151	3.787	0.544
0.50	17.258	33.278	45.281	49.633	73.409	179.71	2.881	3.221	5.867	3.591	0.557
0.75	16.543	32.372	44.061	46.063	62.636	175.69	3.055	3.030	5.572	3.380	0.579
1.0	15.51	31.329	42.912	43.679	53.424	172.59	3.218	2.859	5.316	3.192	0.602

Table 6 Calculated quasi-longitudinal wave velocities (v_p) and quasi-shear wave velocities (v_s) (in km s^{-1} units). Here, the subscripts max and min indicate maximum and minimum velocities. Calculated single-crystal azimuthal seismic anisotropy for longitudinal (A_P) and shear (A_S) waves (in %), Gruneisen parameter (γ) (dimensionless), Pugh's ratio (k) (dimensionless) and melting temperature (T_m) (in Kelvin) for $Na_2Si_{1-x}Ge_xO_3$ ($x = 0.0, 0.25, 0.50, 0.75, 1.0$)

x	$v_{p_{max}}$	$v_{p_{min}}$	$v_{s_{max}}$	$v_{s_{min}}$	$\bar{V}_{P_{VRH}}$	$\bar{V}_{S_{VRH}}$	A_P	A_S	γ	k	μ_m	T_m
0.0	7.017	6.172	4.463	2.864	6.491	3.615	13.02	49.21	1.63	1.89	1.2446	877.626 ± 300
0.25	6.592	5.911	4.210	2.565	6.151	3.400	11.07	48.38	1.66	1.94	1.2652	851.396 ± 300
0.50	6.293	5.682	3.989	2.448	5.867	3.217	10.41	47.90	1.68	1.99	1.2929	835.197 ± 300
0.75	5.964	5.276	3.804	2.327	5.572	3.030	12.35	48.76	1.71	2.05	1.2994	807.401 ± 300
1.0	5.681	4.864	3.652	2.196	5.316	2.859	15.37	50.93	1.75	2.12	1.3019	779.682 ± 300

At $x = 0.0$, we have obtained $A_P = 13.02\%$ and $A_S = 49.21\%$. These results are consistent with the results of Belmonte et al.,[28] in which the A_P and A_S values were 15% and 51% respectively for Na_2SiO_3. From Table 6, our A_P and A_S values are relatively high for $x = 0.0, 0.25, 0.50, 0.75, 1.0$, indicating the anisotropic single-crystal elasticity. The highly anisotropic single-crystal elasticity behavior is also confirmed by the large values of C_{11}, C_{22} and C_{33} as compared to the other elastic stiffness tensors. Considerably large values of C_{11}, C_{22} and C_{33} with respect to the other elastic constant tensors also show that $Na_2Si_{1-x}Ge_xO_3$ are more resistant to axial compression compared to shear deformation. This is further confirmed by the fact that the bulk modulus (B) values given in Table 7 are comparatively larger than the values of shear modulus (G). For internal deformation stability, we have calculated the dimensionless Kleinman coefficient ζ (see Table 5) by employing eqn (6):[76]

$$\zeta = \frac{C_{11} + 8C_{12}}{7C_{11} + 2C_{12}} \tag{6}$$

A Kleinman coefficient in the range of $0 \leq \zeta \leq 1$ determines the stability of the compounds against stretching and bending. ζ closer to 0 indicates a negligible contribution of bond bending to resist external stress. From the calculated results, it has been observed that the mechanical strength of the studied compounds was mostly governed by bond stretching or contracting rather than bending of bonds. For machinability purposes and practical applicability, we have performed the calculation of the machinability index μ_m, which indicates the feasibility of machinery applications, cutting forces, plasticity and lubricating properties, and the melting temperature T_m (see Table 6). The formulae adopted for μ_m and T_m calculations are:[77,78]

$$\mu_m = \frac{B}{C_{44}} \tag{7}$$

$$T_m = 354 + 4.5\left(\frac{2C_{11} + C_{33}}{3}\right) \pm 300 \tag{8}$$

The calculated μ_m are all in an acceptable range for machinability, lower feed forces, mediocre lubricating properties and high strain value. The calculated T_m at $x = 0.0$ is comparable to the experimental melting temperature ($T_m = 810$ °C) of sodium orthosilicate ($2Na_2O \cdot SiO_2$) estimated by Meshalkin et al.[79] where the investigation was performed at near-liquidus phase equilibria in 33–58.5 mol% SiO_2.

In Table 7, we have reported the calculated elastic moduli and Poisson's ratio for different x values which are all estimated in terms of the Voigt[80] (uniform strain assumption), Reuss[81] (uniform stress assumption) and Hill assumptions.[82] When the x value increases, the elastic moduli decrease while the Poisson's ratio increases, suggesting that the systems being studied are under tensile deformation rather than compressive. The increasing Poisson's ratio with x indicates the ductile nature, further confirmed by the increase in Pugh ratio $\left(k = \dfrac{G}{B}\right)$ (see Table 6). The critical value for the transition from ductile materials to brittle ones is 1.75 (i.e., $k > 1.75$ indicates a ductile material). It is well known that in crystallography the isotropy or anisotropy of a material plays an important role. Making use of the elastic stiffness tensors and elastic moduli, we have calculated the two anisotropic factors A_{an} and A^U (see Table 5) given by:[83]

$$A_{an} = \frac{4C_{11}}{C_{11} + C_{33} - 2C_{13}} \tag{9}$$

$$A^U = 5\frac{G_V}{G_R} + \frac{B_V}{B_R} - 6 \tag{10}$$

Here, A_{an} and A^U represent the elastic anisotropy and the strength of the anisotropy of the materials, respectively. The calculated A_{an} for all values of x are greater than 1, indicating the compounds are elastically anisotropic. For isotropic materials $A_{an} = 1$. The deviation of A^U from zero corresponds to the strength of the anisotropy of the materials. The maximum deviation of A^U from zero is observed at $x = 0.0$ and 1.0; this reveals that Na_2SiO_3 and Na_2GeO_3 are highly anisotropic materials which seems to be the generic feature of glass materials.[84]

One of the main concerns for elastic property calculation is figuring out the average sound velocity v_{av} determined by the transverse (v_t) and longitudinal (v_l) velocities and the Gruneisen parameter (γ). Considering the elastic moduli, density of the compound and Poisson's ratio we perform such calculations:[85]

$$v_{av} = \left[\frac{1}{3}\left(\frac{1}{v_l^3} + \frac{2}{v_t^3}\right)\right]^{\frac{-1}{3}} \tag{11}$$

where $v_l = \sqrt{\dfrac{3B + 4G}{3\rho}}$ and $v_t = \sqrt{\dfrac{G}{\rho}}$.

$$\gamma = \frac{3(1 + \nu)}{2(2 - 3\nu)} \tag{12}$$

where ν is the Poisson's ratio.

Table 7 Calculated elastic moduli (Bulk modulus (B), Young's modulus (Y), and Shear modulus (G) all in GPa units) and Poisson's ratio (ν) (unitless) for $Na_2Si_{1-x}Ge_xO_3$ ($x = 0.0, 0.25, 0.50, 0.75, 1.0$). Here, the subscripts V, R and H represent Voigt, Reuss and Hill assumptions respectively

x	B_V	B_R	B_H	Y_V	Y_R	Y_H	G_V	G_R	G_H	ν_V	ν_R	ν_H
0.0	62.281	62.202	62.241	88.40	79.454	83.968	34.984	30.865	32.925	0.26344	0.28711	0.27516
0.25	60.714	60.402	60.558	83.88	75.882	79.912	33.03	29.398	31.214	0.26974	0.29062	0.28007
0.50	59.569	59.078	59.324	80.617	72.839	76.756	31.628	28.134	29.881	0.27444	0.29451	0.28436
0.75	57.969	56.92	57.444	76.012	68.679	72.366	29.658	26.438	28.048	0.28146	0.29890	0.29004
1.0	56.734	55.001	55.867	71.91	64.463	68.203	27.899	24.705	26.302	0.28875	0.30466	0.29653

The calculated v_t, v_l and v_{av} are given in Table 5. The obtained values show that v_t, v_l and v_{av} are reduced when x increases. The calculated Gruneisen parameters (γ) [see Table 6] describe the vibrational properties which are affected by the change in crystal volume as x increases. The acoustic wave evaluator in solid media (AWESOME)[86] analyzes the phase and group velocities of the compounds (see Fig. 8). It is clear that the seismic velocities estimated by the Christoffel equation are direction dependent. Fig. 8 shows the group velocity of $Na_2Si_{1-x}Ge_xO_3$ as a function of the propagation direction. In this
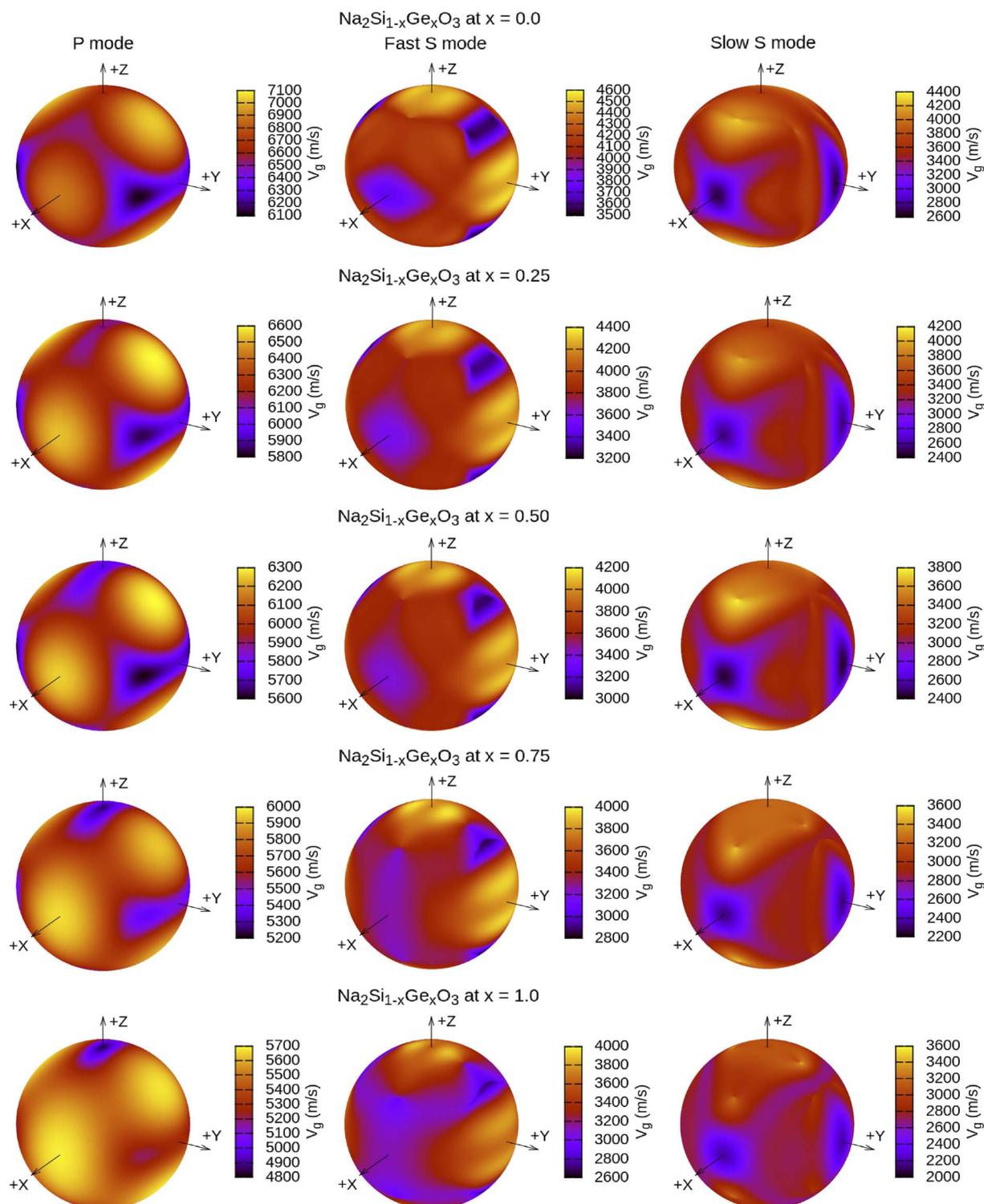
Fig. 8 3-Dimensional plot of group velocity as a function of propagation direction for the p-mode and two s-mode (fast and slow) waves obtained from the Christoffel determinant for $Na_2Si_{1-x}Ge_xO_3$ (x = 0.0, 0.25, 0.50, 0.75, 1.0). Here, v_g are in m s^{-1} units.

study, we have calculated the group velocities of p-mode, fast s-mode and slow s-mode waves under different doping concentration (x). In p-waves or compressional waves, the vibrations of atoms are in the direction of wave propagation and as a result p-waves travel faster as compared to s-waves or shear waves where atoms oscillate perpendicular to the direction of propagation. The main difference between these two waves is that p-waves cause the studied materials to compress and expand along the direction of propagation, while the s-waves have greater amplitude and produce vertical and horizontal vibration, and as a result s-waves are more destructive to the mechanical stability. At $x = 0.0$, for p-mode the maximum velocity ($v_{p_{\max}}$) is 7017 m s^{-1} along [1 1 0] and the minimum velocity ($v_{p_{\min}}$) is 6127 m s^{-1} along [0 1 1]. This implies that the compound being investigated is more dense along [0 1 1], while along the [1 1 0] direction, the density is a minimum for $x = 0.0$. From Table 6, we can observe that $v_{p_{\max}}$ decreases with x, this shows that when the concentration of Ge atoms increases, the compound being investigated has higher density. And the directions for higher and lower density regions are presented in Fig. 8. For the two s-mode seismic waves, $v_{s_{\text{fast}}}$ and $v_{s_{\text{slow}}}$, the maximum velocities are along [0 1 0] and [0 0 1] respectively, while the minimum velocities are along [0 1 1] and [0 1 0] respectively. Clearly, from the equation $v_p = v_g \Psi$, where Ψ is the power flow angle, we can find that the distinction between fast and slow s-modes is due to the phase velocity and therefore, referring to Fig. 8, we observed that for different x values the velocity of the fast s-mode is always higher than that of the slow s-mode.

3.4 Piezoelectric properties

Piezoelectric properties have attracted tremendous research interest due to the green method of energy conversion. Piezoelectric materials are future energy materials that can be practically implemented in actuators, sensors, medical tools for monitoring heartbeats and breathing, and many more.[87–90] Piezoelectric properties of a material emerge as a result of applied mechanical stress that gives rise to atomic scale polarization. The direct 'e' and converse 'd' piezoelectric tensors measure the variation of polarization 'P' induced by strain (η) and the η generated by an external electric field (E) at constant electric field and stress, respectively.

At constant field,

$$P = e\eta \tag{13}$$

At constant stress,

$$\eta = d^{\text{T}} E \tag{14}$$

This calculation is based on computing the intensity of polarization induced by strain. Cartesian polarization components are expressible in terms of strain tensors, given by:

$$P_i = \sum_{\nu} e_{i\nu} \eta_{\nu}$$
$$\text{where } e_{i\nu} = \left(\frac{\delta P_i}{\delta \eta_{\nu}} \right)_E \tag{15}$$

Here, $i = x, y, z$; $\nu = 1, 2, 3, 4, 5, 6$ ($1 = xx$, $2 = yy$, $3 = zz$, $4 = yz$, $5 = xz$, and $6 = xy$); η is the strain tensor; and E is the induced electric field. In this calculation, the Berry phase (BP) approach is adopted in which direct piezoelectric constants are given in terms of numerical first derivatives of the BP φ_l with respect to strain.[91–94]

$$e_{i\nu} = \frac{|e|}{2\pi V} \sum_l a_{li} \frac{\delta \varphi_l}{\delta \eta_{\nu}} \tag{16}$$

where a_{li} is the ith Cartesian component of the lth direct lattice basis vector a_l. The derivative $\frac{\delta \varphi_l}{\delta \eta_{\nu}}$ is computed numerically by applying finite strains to the crystal lattice. The direct and converse piezoelectric tensors are closely related; the relationship between the tensors is given by:

$$e = dC,$$
$$d = eS \tag{17}$$

where C is the fourth-rank elastic tensor of energy second derivatives with respect to pairs of deformations and $S = C^{-1}$ is the fourth-rank compliance tensor.

The main aim of calculating the piezoelectric properties is to obtain the direct and converse piezoelectric response of the studied compounds, and compare these results with commonly used and standard piezoelectric materials such as quartz (SiO$_2$). The strain (η) along different directions results in the disruption of the structure which will patently distort the negative cloud of electrons surrounding the positive nuclei. This small separation leads to an electric field between them, and as such polarization is developed which can be manipulated to give novel piezoelectric properties. In Tables 8 and 9, we report the direct and converse piezoelectric response for Na$_2$Si$_{1-x}$Ge$_x$O$_3$. Tarumi et al.[95] found experimentally that for α-quartz (α-SiO$_2$), the piezoelectric constant was largest along the x-axis due to strain η_{xx} with a value $e_{11} = 0.15$ C m^{-2} at room temperature, and at 5 K, the reported piezoelectric constant was 0.07 C m^{-2}. From these calculations, it was clarified that the studied compounds had a better response towards piezoelectricity as compared to SiO$_2$. For each case (i.e., at $x = 0.0, 0.25, 0.50, 0.75, 1.0$), the maximum piezoelectric responses induced are along the z-axis by strain η_{yy}, i.e., for piezoelectric constant e_{32}. The calculated direct piezoelectric constant first increases with doping concentration x, and is a maximum at $x = 0.50$ with $e_{32} = 0.308$ C m^{-2} which then decreases. Moreover, we can observe a noticeable piezoelectric response along the y-axis induced by strain η_{yz} (i.e., e_{24}) and also along the z-axis again but induced by strain η_{xx} (i.e., e_{31}). Considering how doping concentration affects the piezoelectric constant, the maximum piezoelectric response possible at $x = 0.50$ will be due to the equilibrium concentration between Ge and Si. This suggests that the piezoelectric properties of the studied compounds are significantly affected by the motion of both Si and Ge atoms. However, the overall piezoelectric response was better for Na$_2$GeO$_3$ than for Na$_2$SiO$_3$. Computed converse piezoelectric constants or piezoelectric strain constants ($d_{i\nu}$) that describe the situation where strain develops under an applied electric field are the result of coupling of the direct piezoelectric and compliance constants. The maximum values obtained at d_{32}

Table 8 Direct piezoelectric constants of $Na_2Si_{1-x}Ge_xO_3$ ($x = 0.0, 0.25, 0.50, 0.75, 1.0$) (in C m^{-2} units)

x	e_{15}	e_{16}	e_{21}	e_{22}	e_{23}	e_{24}	e_{31}	e_{32}	e_{33}	e_{34}
0.0	0.103	0.001	—	0.003	−0.001	0.145	0.140	0.221	−0.582	—
0.25	—	0.008	0.015	−0.011	−0.010	0.132	0.156	0.262	−0.715	0.006
0.50	—	0.015	0.029	−0.017	−0.015	0.134	0.123	0.308	−0.768	0.028
0.75	—	0.006	0.023	−0.014	−0.006	0.127	0.192	0.290	−0.909	0.012
1.0	—	—	—	—	—	0.104	0.182	0.287	−1.015	—

Table 9 Converse piezoelectric constants of $Na_2Si_{1-x}Ge_xO_3$ ($x = 0.0, 0.25, 0.50, 0.75, 1.0$) (in pm V^{-1} units)

x	d_{15}	d_{16}	d_{21}	d_{22}	d_{23}	d_{24}	d_{31}	d_{32}	d_{33}	d_{34}
0.0	2.930	0.043	−0.014	0.048	−0.020	2.905	1.161	4.688	−7.263	0.003
0.25	—	—	0.230	−0.175	−0.110	2.757	1.514	6.032	−9.855	0.267
0.50	—	—	0.443	−0.280	−0.229	2.916	0.894	7.747	−11.587	1.214
0.75	—	—	0.380	−0.307	−0.105	2.872	2.734	8.150	−15.369	0.593
1.0	—	—	—	—	—	2.416	3.955	9.039	−19.494	−0.002

for different doping concentrations are the result of softening of the C_{32} elastic constants upon relaxation. The reported d_{32} values increase with x with the highest value of 9.039 pm V^{-1} at $x = 1.0$. In conclusion, we can say that the calculated piezoelectric constants for $Na_2Si_{1-x}Ge_xO_3$ are fairly low in comparison to some ferroelectric materials such as SrTiO$_3$ with $I4cm$ space group that shows a piezoelectric response of $e_{33} = 8.82$ C m^{-2}.[96] Therefore, to utilize $Na_2Si_{1-x}Ge_xO_3$ for practical and efficient piezoelectric devices, more rigorous research so as to further enhance its piezoelectric responses is vital. From the surveyed literature, we have found that utilizing low dimensional (LD) materials for piezoelectric materials could enhance the piezoelectric response compared to their bulk forms.[97] Recently, Wang et al.[98] reported the piezoelectric response for 2-D SnS$_2$ nanosheets with thickness of ~4 nm and pointed out that the piezoelectric responses reduce with an increase in the thickness of the nanosheets. They obtained an effective out-of-plane piezoelectric response of 2 ± 0.22 pm V^{-1}. This value is comparable to our calculated converse piezoelectric constant d_{24} where our observed values are within the range of 2.4 to 3 pm V^{-1}.

4 Conclusions

In summary, we have studied the structural, electronic, mechanical and piezoelectric properties of complex glass-like $Na_2Si_{1-x}Ge_xO_3$ by using DFT calculations. We have shown that the structural and the electronic properties of the studied compounds are mostly defined by the presence of silicon and germanium. Also, doping with heavier elements tuned the wide band gap to a medium one. Our calculations of phonon dispersion curves, formation energy and elastic tensor constants revealed that the transformation of $Na_2SiO_3 \rightarrow Na_2GeO_3$ is practically possible by preserving dynamical as well as mechanical stability. The calculated machinability index and melting temperature have shown that the compounds under investigation are at an acceptable machinability level and can be utilised in a high temperature range. We observe maximum piezoelectric

responses along the z-axis, $i.e.$, e_{32}, for all structures and these values are higher than that of the standard piezoelectric material SiO$_2$. However, our observed maximum direct piezoelectric constant $e_{32} = 0.308$ C m^{-2} at $x = 0.50$ seems to be low as compared to the ferroelectric material SrTiO$_3$. So, for practical application of $Na_2Si_{1-x}Ge_xO_3$ as a piezoelectric component in devices, we need rigorous research to enhance the efficiency.

Conflicts of interest

The authors declare no conflicts of interest.

Acknowledgements

References

1 J. Y. Tsao, S. Chowdhury, M. A. Hollis, D. Jena, N. M. Johnson, K. A. Jones, R. J. Kaplar, S. Rajan, C. G. Van

de Walle, E. Bellotti, C. L. Chua, R. Collazo, M. E. Coltrin, J. A. Cooper, K. R. Evans, S. Graham, T. A. Grotjohn, E. R. Heller, M. Higashiwaki, M. S. Islam, P. W. Juodawlkis, M. A. Khan, A. D. Koehler, J. H. Leach, U. K. Mishra, R. J. Nemanich, R. C. N. Pilawa-Podgurski, J. B. Shealy, Z. Sitar, M. J. Tadjer, A. F. Witulski, M. Wraback and J. A. Simmons, *Adv. Electron. Mater.*, 2018, **4**, 1600501.

2 R. Woods-Robinson, Y. Han, H. Zhang, T. Ablekim, I. Khan, K. A. Persson and A. Zakutayev, *Chem. Rev.*, 2020, **120**, 4007–4055.

3 L.-g. Liu, *Geophys. Res. Lett.*, 1987, **14**, 1079–1082.

4 J. M. D. Coey, *Mössbauer Spectroscopy Applied to Inorganic Chemistry*, Springer US, Boston, MA, 1984, pp. 443–509.

5 L. Zhu, Y. R. Zeng, J. Wen, L. Li and T. M. Cheng, *Electrochim. Acta*, 2018, **292**, 190–198.

6 Y. Ren, Y. Zhang, Y. Gu and Q. Zeng, *Prog. Org. Coat.*, 2017, **112**, 225–233.

7 M. Lancry, E. Régnier and B. Poumellec, *Prog. Mater. Sci.*, 2012, **57**, 63–94.

8 S. Kaya, M. Cresswell and A. R. Boccaccini, *Mater. Sci. Eng., C*, 2018, **83**, 99–107.

9 E. Borsella, E. Cattaruzza, G. De Marchi, F. Gonella, G. Mattei, P. Mazzoldi, A. Quaranta, G. Battaglin and R. Polloni, *J. Non-Cryst. Solids*, 1999, **245**, 122–128.

10 J. O. Bockris, J. D. Mackenzie and J. A. Kitchener, *Trans. Faraday Soc.*, 1955, **51**, 1734.

11 C. A. Faick and A. N. Finn, *J. Am. Ceram. Soc.*, 1931, **14**, 518–528.

12 L. Shartsis, S. Spinner and W. Capps, *J. Am. Ceram. Soc.*, 1952, **35**, 155–160.

13 T. Uchino, M. Iwasaki, T. Sakka and Y. Ogata, *J. Phys. Chem.*, 1991, **95**, 5455–5462.

14 Y. Kowada and D. Ellis, *Adv. Quantum Chem.*, Academic Press, 1998, vol. 29, pp. 233–251.

15 A. K. Varshneya and J. C. Mauro, *Fundamentals of Inorganic Glasses*, Elsevier, 2019, pp. 1–18.

16 G. Agrawal, *Nonlinear Fiber Optics*, Elsevier, 2013, pp. 457–496.

17 *Application of Silica Glasses in Practice*, ed. I. Fanderlik, Elsevier, 1991, vol. 11, pp. 271–300.

18 C. Li, C. Liu, W. Wang, Z. Mutlu, J. Bell, K. Ahmed, R. Ye, M. Ozkan and C. S. Ozkan, *Sci. Rep.*, 2017, **7**, 917.

19 L. Granados, R. Morena, N. Takamure, T. Suga, S. Huang, D. R. McKenzie and A. Ho-Baillie, *Mater. Today*, 2021, **47**, 131–155.

20 M. Mir, M. N. Ali, J. Sami and U. Ansari, *Adv. Mater. Sci. Eng.*, 2014, **2014**, 1–17.

21 R. Morrell, *Comprehensive Composite Materials*, Elsevier, 2000, pp. 1–24.

22 J. T. Randall, H. P. Rooksby and B. S. Cooper, *Z. Kristallogr. - Cryst. Mater.*, 1930, **75**, 196–214.

23 W. H. Zachariasen, *J. Am. Chem. Soc.*, 1932, **54**, 3841–3851.

24 I. Farnan, *Nature*, 1997, **390**, 14–15.

25 K. Baral, A. Li and W.-Y. Ching, *J. Phys. Chem. A*, 2017, **121**, 7697–7708.

26 P. Richet, B. O. Mysen and D. Andrault, *Phys. Chem. Miner.*, 1996, **23**, 157–172.

27 W. S. McDonald and D. W. J. Cruickshank, *Acta Crystallogr.*, 1967, **22**, 37–43.

28 D. Belmonte, C. Gatti, G. Ottonello, P. Richet and M. V. Zuccolini, *J. Phys. Chem. A*, 2016, **120**, 8881–8895.

29 C. Cuautli, I. Romero-Ibarra, J. Vazquez-Arenas and M. Galvan, *Fuel*, 2021, **298**, 120840.

30 F. Liu, S. Garofalini, R. King-Smith and D. Vanderbilt, *Chem. Phys. Lett.*, 1993, **215**, 401–404.

31 G. Greaves, *J. Non-Cryst. Solids*, 1985, **71**, 203–217.

32 Y. Cao, A. N. Cormack, A. G. Clare, B. Bachra, A. C. Wright, R. N. Sinclair and A. C. Hannon, *J. Non-Cryst. Solids*, 1994, **177**, 317–323.

33 D. W. Matson, S. K. Sharma and J. A. Philpotts, *J. Non-Cryst. Solids*, 1983, **58**, 323–352.

34 H. Maekawa, T. Maekawa, K. Kawamura and T. Yokokawa, *J. Non-Cryst. Solids*, 1991, **127**, 53–64.

35 G. N. Greaves, S. J. Gurman, C. R. A. Catlow, A. V. Chadwick, S. Houde-Walter, C. M. B. Henderson and B. R. Dobson, *Philos. Mag. A*, 1991, **64**, 1059–1072.

36 M. G. Mortuza, R. Dupree and D. Holland, *J. Non-Cryst. Solids*, 2001, **281**, 108–116.

37 L. Olivier, X. Yuan, A. N. Cormack and C. Jäger, *J. Non-Cryst. Solids*, 2001, 53–66.

38 A. Meyer, J. Horbach, W. Kob, F. Kargl and H. Schober, *Phys. Rev. Lett.*, 2004, **93**, 027801.

39 B. Gee and H. Eckert, *J. Phys. Chem.*, 1996, **100**, 3705–3712.

40 G. N. Greaves, A. Fontaine, P. Lagarde, D. Raoux and S. J. Gurman, *Nature*, 1981, **293**, 611–616.

41 Y. Foucaud, M. Badawi, L. O. Filippov, O. Barres, I. V. Filippova and S. Lebègue, *Chem. Sci.*, 2019, **10**, 9928–9940.

42 K. Baral and W. Y. Ching, *J. Appl. Phys.*, 2017, **121**, 245103.

43 K. Baral, A. Li and W.-Y. Ching, *J. Phys. Chem. A*, 2017, **121**, 7697–7708.

44 S. Kikuchi, N. Koga, H. Seino and S. Ohno, *J. Nucl. Sci. Technol.*, 2016, **53**, 682–691.

45 A. Bunde, M. Ingram, P. Maass and K. Ngai, *J. Non-Cryst. Solids*, 1991, **131–133**, 1109–1112.

46 R. L. McGreevy and L. Pusztai, *Mol. Simul.*, 1988, **1**, 359–367.

47 S. Ispas, M. Benoit, P. Jund and R. Jullien, *Phys. Rev. B: Condens. Matter Mater. Phys.*, 2001, **64**, 214206.

48 A. Pandey, P. Biswas and D. A. Drabold, *Phys. Rev. B: Condens. Matter Mater. Phys.*, 2015, **92**, 155205.

49 Y. Ginetti, *Bull. Soc. Chim. Belg.*, 2010, **63**, 460–469.

50 H. Vllenkle, A. Wittmann and H. Nowotny, *Monatsh. Chem.*, 1971, **102**, 964–970.

51 D. W. J. Cruickshank, A. Kálmán and J. S. Stephens, *Acta Crystallogr., Sect. B: Struct. Crystallogr. Cryst. Chem.*, 1978, **34**, 1333–1334.

52 A. R. West and A. J. Blake, *J. Mater. Sci.*, 1976, **11**, 801–808.

53 R. Zosiamliana, Lalrinkima, B. Chettri, G. Abdurakhmanov, M. P. Ghimire and D. P. Rai, *RSC Adv.*, 2022, **12**, 12453–12462.

54 R. Dovesi, A. Erba, R. Orlando, C. M. Zicovich-Wilson, B. Civalleri, L. Maschio, M. Rérat, S. Casassa, J. Baima,

S. Salustro and B. Kirtman, *Wiley Interdiscip. Rev. Comput. Mol. Sci.*, 2018, **8**, e1360.

55 J. P. Perdew, K. Burke and M. Ernzerhof, *Phys. Rev. Lett.*, 1997, **78**, 1396.

56 D. Vilela Oliveira, J. Laun, M. F. Peintinger and T. Bredow, *J. Comput. Chem.*, 2019, **40**, 2364–2376.

57 M. F. Peintinger, D. V. Oliveira and T. Bredow, *J. Comput. Chem.*, 2013, **34**, 451–459.

58 H. J. Monkhorst and J. D. Pack, *Phys. Rev. B: Solid State*, 1976, **13**, 5188–5192.

59 A. Grund and M. Pizy, *Acta Crystallogr.*, 1952, **5**, 837–840.

60 F. D. Murnaghan, *Am. J. Math.*, 1937, **59**, 235.

61 F. Birch, *Phys. Rev.*, 1947, **71**, 809–824.

62 D. Kalita, M. Ram, N. Limbu, R. Kalita and A. Saxena, *J. Solid State Chem.*, 2022, **310**, 122999.

63 P. Vashishta, R. K. Kalia, J. P. Rino and I. Ebbsjö, *Phys. Rev. B: Condens. Matter Mater. Phys.*, 1990, **41**, 12197–12209.

64 J. Sarnthein, A. Pasquarello and R. Car, *Phys. Rev. Lett.*, 1995, **74**, 4682–4685.

65 K. N. Subedi, V. Botu and D. A. Drabold, *Phys. Rev. B*, 2021, **103**, 134202.

66 R. Greegor, F. Lytle, J. Kortright and A. Fischer-Colbrie, *J. Non-Cryst. Solids*, 1987, **89**, 311–325.

67 W. Y. Ching, R. A. Murray, D. J. Lam and B. W. Veal, *Phys. Rev. B: Condens. Matter Mater. Phys.*, 1983, **28**, 4724–4735.

68 G. H. Sigel, *Treatise on Materials Science and Technology*, Academic press, INC, 1977, vol. 12, pp. 5–89.

69 Y. Wang, A. Zavabeti, F. Haque, B. Y. Zhang, Q. Yao, L. Chen, D. Chen, Y. Hu, N. Pillai, Y. Liu, K. A. Messalea, C. Yang, B. Jia, D. M. Cahill, Y. Li, C. F. McConville, J. Z. Ou, L. Kong, X. Wen and W. Yang, *Mater. Today*, 2022, **55**, 21–28.

70 W. Perger, J. Criswell, B. Civalleri and R. Dovesi, *Comput. Phys. Commun.*, 2009, **180**, 1753–1759.

71 A. Erba, A. Mahmoud, R. Orlando and R. Dovesi, *Phys. Chem. Miner.*, 2014, **41**, 151–160.

72 F. Mouhat and F.-X. Coudert, *Phys. Rev. B: Condens. Matter Mater. Phys.*, 2014, **90**, 224104.

73 Q. Guo, K. C. Lau and R. Pandey, *J. Phys. Chem. C*, 2019, **123**, 4674–4681.

74 C. Acoustics and M. J. P. Musgrave, *Geophys. J. R. Astron. Soc.*, 1971, **24**, 207–211.

75 W.-Y. Zhou, Z. Ren, J. S. Zhang, B. Chen, M. Hao, T. Ohuchi, L. Miyagi, D. Zhang, E. E. Alp, B. Lavina and B. Schmandt, *Earth Planet. Sci. Lett.*, 2021, **565**, 116955.

76 L. Kleinman, *Phys. Rev.*, 1962, **128**, 2614–2621.

77 M. Fine, L. Brown and H. Marcus, *Scr. Metall.*, 1984, **18**, 951–956.

78 H. Zhang, Y. Tang, X. Zhong, Y. Zhang, H. Song, J. Wang and Q. Wang, *Mater. Res. Express*, 2019, **6**, 056507.

79 A. Meshalkin and A. Kaplun, *Russ. J. Inorg. Chem.*, 2003, **48**, 1567–1569.

80 W. Voigt, *Lehrbuch der Kristallphysik*, References – Scientific Research Publishing, Teubner Verlag, Leipzig, 1928.

81 A. Reuss, *J. Appl. Math. Mech.*, 1929, **9**, 49–58.

82 R. Hill, *Proc. Phys. Soc., London, Sect. A*, 1952, **65**, 349–354.

83 J. P. Watt and L. Peselnick, *J. Appl. Phys.*, 1980, **51**, 1525–1531.

84 A. Gujral, L. Yu and M. Ediger, *Curr. Opin. Solid State Mater. Sci.*, 2018, **22**, 49–57.

85 A. C. Holt and M. Ross, *Phys. Rev. B: Condens. Matter Mater. Phys.*, 1970, **1**, 2700–2705.

86 D. Muñoz-Santiburcio, A. Hernández-Laguna and J. I. Soto, *Comput. Phys. Commun.*, 2015, **192**, 272–277.

87 D. Damjanovic and R. E. Newnham, *J. Intell. Mater. Syst. Struct.*, 1992, **3**, 190–208.

88 E. Aksel and J. L. Jones, *Advances in lead-free piezoelectric materials for sensors and actuators*, 2010.

89 M. T. Chorsi, E. J. Curry, H. T. Chorsi, R. Das, J. Baroody, P. K. Purohit, H. Ilies and T. D. Nguyen, *Adv. Mater.*, 2019, **31**, 1802084.

90 A. Zaszczyńska, A. Gradys and P. Sajkiewicz, *Polymers*, 2020, **12**, 2754.

91 Y. Noel, C. M. Zicovich-Wilson, B. Civalleri, P. D'Arco and R. Dovesi, *Phys. Rev. B: Condens. Matter Mater. Phys.*, 2001, **65**, 014111.

92 R. Resta, *Rev. Mod. Phys.*, 1994, **66**, 899–915.

93 R. D. King-Smith and D. Vanderbilt, *Phys. Rev. B: Condens. Matter Mater. Phys.*, 1993, **47**, 1651–1654.

94 D. Vanderbilt, *J. Phys. Chem. Solids*, 2000, **61**, 147–151.

95 R. Tarumi, K. Nakamura, H. Ogi and M. Hirao, *J. Appl. Phys.*, 2007, **102**, 113508.

96 A. Erba, K. E. El-Kelany, M. Ferrero, I. Baraille and M. Rérat, *Phys. Rev. B: Condens. Matter Mater. Phys.*, 2013, **88**, 035102.

97 Y. Wang, X. Guo, L. H. Li, J. Zhang, G. K. Li, A. Zavabeti and Y. Li, *ACS Appl. Nano Mater.*, 2022, DOI: **10.1021/acsanm.2c01871**.

98 Y. Wang, L.-M. Vu, T. Lu, C. Xu, Y. Liu, J. Z. Ou and Y. Li, *ACS Appl. Mater. Interfaces*, 2020, **12**, 51662–51668.